Spatial and Spectral Unmixing Using the Beta Compositional Model

Xiaoxiao Du, *Student Member, IEEE,* Alina Zare, *Senior Member, IEEE,*
Paul Gader, *Fellow, IEEE,* and Dmitri Dranishnikov

Abstract—This paper introduces the beta compositional model (BCM) for hyperspectral unmixing and four algorithms for unmixing given the BCM. Hyperspectral unmixing estimates the proportion of each endmember at every pixel of a hyperspectral image. Under the BCM, each endmember is a random variable distributed according to a beta distribution. By using a beta distribution, spectral variability is accounted for during unmixing, the reflectance values of each endmember are constrained to a physically realistic range, and skew can be accounted for in the distribution. Spectral variability is incorporated to increase hyperspectral unmixing accuracy. Two BCM-based spectral unmixing approaches are presented: BCM-spectral and BCM-spatial. For each approach, two algorithms, one based on quadratic programming (QP) and one using a Metropolis–Hastings (MH) sampler, are developed. Results indicate that the proposed BCM unmixing algorithms are able to successfully perform unmixing on simulated data and real hyperspectral imagery while incorporating endmember spectral variability and spatial information.

Index Terms—Beta compositional model (BCM), endmember, hyperspectral, spatial–spectral, spectral variability, unmixing.

I. INTRODUCTION

HYPERSPECTRAL unmixing estimates the proportion of each endmember at every pixel of the image. In hyperspectral imagery, the reflectance value of an endmember may vary due to environmental factors such as atmospheric effects, illumination, moisture conditions, and inherent spectral variability of the material itself, such as the variations in biophysical and biochemical composition in vegetation [1]. In this paper, in order to increase the accuracy in hyperspectral unmixing, spectral variability is taken into account.

In the literature, there are two dominant categories for endmember representation that take into account spectral variability [2]: 1) endmembers represented as a discrete set, or 2) endmembers represented using a continuous distribution. Methods that make use of the *endmembers as sets* representation include support vector machine approaches [3], [4], the Bayesian spectral mixture analysis method (BSMA) [1], multiple endmember spectral mixture analysis (MESMA) [5], Multiple-Endmember

Linear Spectral Unmixing Model (MELSUM) [6], Auto-Monte Carlo Unmixing (AutoMCU) [7], endmember bundles [8], and band weighting or transformation approaches [9]–[11]. Previous methods that make use of the *endmember as distributions* representation include those that are based on the normal compositional model (NCM) [12]–[15] and the higher-order moments approach [16]. Fig. 1 provides a summary diagram of these approaches.

NCM uses the Gaussian distribution to represent each endmember (primarily due to mathematical simplicity). However, the NCM allows for endmember samples to range outside the interval of [0, 1] and cannot represent skew in the endmember distributions. Generally, the reflectance values of spectra are found in the interval of [0, 1] and, often, when manually examining the distribution of material reflectance values, a nonzero skewness value is observed. Thus, in this paper, the beta distribution is considered to represent each endmember. The use of the beta distribution constrains endmember samples to be in a physically realistic range, incorporate skew, and represent spectral variability. Furthermore, spatial and spectral unmixing algorithms based on using the beta distribution representation for endmembers are presented.

In the following, Section II provides motivation for the beta compositional model (BCM). Section III introduces the BCM. Section IV develops the proposed algorithms based on the BCM. Section V presents unmixing results on both simulated and measured hyperspectral imagery. Section VI provides a summary and discussion of future work.

II. MOTIVATION FOR THE BETA DISTRIBUTION

In order to investigate whether the beta distribution is a good fit for endmember spectra, comparisons between hyperspectral data and their representation using the beta distribution were made. Specifically, quantile–quantile (Q–Q) plots [17] were used to visualize the difference between the beta distribution representation, the Gaussian distribution representation (for comparison to the NCM), and the original data. A Q–Q plot compares the similarity of two distributions by plotting their inverse cumulative distribution values at regular intervals versus one another. It was found that, for some materials, the beta distribution provided a better fit to measured hyperspectral data. For example, 300 pixels of grass were extracted from a hyperspectral image collected over Long Beach, MS at the University of Southern Mississippi Gulfpark campus [18]. For each band of this extracted data, the parameters for a Gaussian distribution and a beta distribution were estimated using a maximum-likelihood
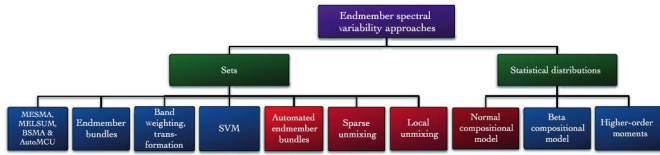
Fig. 1. Summary of spectral unmixing and endmember estimation algorithms that account for spectral variability. Methods shown in blue perform spectral unmixing. Methods in red perform unmixing and endmember estimation.
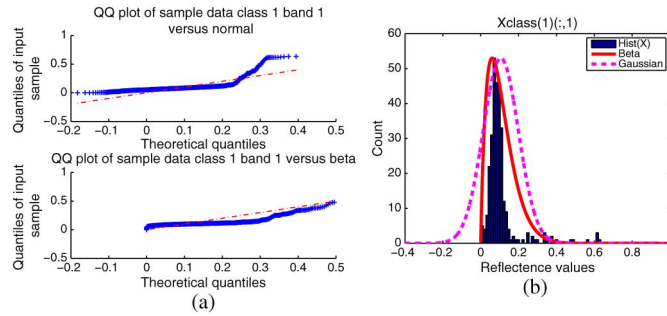

Fig. 2. Q–Q plot and histogram of grass endmember. (a) Q–Q plot for grass endmember at 368 nm wavelength. (b) Histogram of grass endmember spectra values at 368 nm wavelength and comparison to fitted Gaussian and beta distributions.

approach. Specifically, in the current implementation, MATLAB's *normfit* and *betafit* functions are used [19]. In Fig. 2(a), the Q–Q plots comparing the beta distribution to the histogram of the measured data and comparing the Gaussian distribution to the histogram of the measured data at the 368 nm wavelength are shown. In these plots, the x-value of a point corresponds to the quantile of the fitted beta or Gaussian distribution and the y-value is the quantile of the sample data. Thus, if the fitted distribution and the sample quantiles are equal, the Q–Q plot will be the $45°$ line $y = x$. Furthermore, Fig. 2(b) shows the fitted beta and Gaussian distributions plotted over the histogram of the grass spectral values at wavelength 368 nm. Both of these figures illustrate that, for some materials, such as the grass example shown here, the beta distribution may provide a better fit over the Gaussian distribution.

In addition, two quantitative measurements, root mean square (rms) and Kullback–Leibler divergence (KL-Divergence) are used to compare the beta approximation and Gaussian approximation versus the original histogram for a variety of materials extracted from the University of Pavia hyperspectral data set, PaviaU [20]. The Pavia University data were collected over an urban area of Pavia, in northern Italy, by the Reflective Optics System Imaging Spectrometer (ROSIS) on July 8, 2002. The image contains 610×340 pixels with 103 bands. The ROSIS sensor collected the data over the range 430–850 nm wavelengths, at a 4-nm spectral sampling interval. In both methods, the data histograms and the beta and Gaussian approximations are binned from 0 to 1 with an increment of 0.0001. Then, the rms difference between the true data histogram value and the approximated beta and Gaussian value can be calculated. If the rms of the beta distribution is smaller than the rms of the Gaussian, the beta approximation fits the data better. Similarly, the KL-Divergence [21] can be used to measure the difference between two probability distributions P and Q.
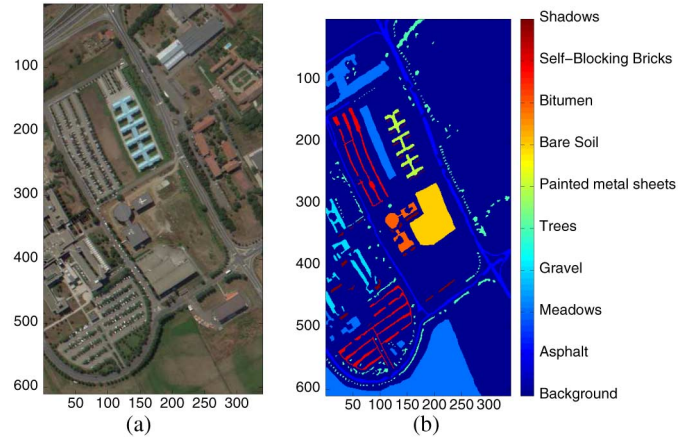

Fig. 3. Pavia University hyperspectral data set. RGB image is constructed using wavelengths of 699.1, 564.6, and 483 nm for the red, green, and blue channels, respectively. (a) RGB image and (b) ground truth.

Specifically, the KL-Divergence of Q from P, denoted $KL(P\|Q)$, calculates the average additional amount of information that is required for distribution Q to match distribution P, i.e., the information lost when Q is used to approximate P. $KL(P\|Q)$ can be written as follows:

$$KL(p\|q) = -\int p(x) \ln \frac{q(x)}{p(x)} dx. \qquad (1)$$

In our comparisons, the "true" distribution values are represented as $p(x)$ where x refers to the endmember reflectance values in one wavelength. Endmember spectra were manually selected from the PaviaU data set.

Fig. 3 shows an RGB image of this hyperspectral scene and the ground truth labels. The differences between beta approximation and Gaussian approximation versus the true data histograms are calculated for every band. The number of times the beta distribution approximation provided a better fit over a Gaussian distribution approximation was recorded. Table I lists the number of samples extracted from the data, comparison results using the rms, and the KL-Divergence measurements. It can be observed that for some endmembers, a beta distribution provides a better fit. In particular, in the Pavia University data, it seems that the dark materials were better represented using a beta distribution (e.g., asphalt, bare soil). This is likely due to the fact that the Gaussian distribution is not truncated and has likelihood over negative reflectance values for dark materials. In contrast, the beta distribution is defined only of the interval [0, 1].

Future work will include determining, for each material, what distribution provides the best representation.

III. BETA COMPOSITIONAL MODEL

The common *linear mixing model* (LMM) [22], [23] represents each endmember as a single spectrum and each pixel as a convex combination of the endmembers. In this paper, endmembers are represented using beta distributions. The BCM [24] assumes a univariate beta distribution for each endmember at each spectral band

$$e_{md} \sim B(\cdot|\alpha_{md}, \beta_{md}) \qquad (2)$$

TABLE I
RMS AND KL-DIVERGENCE MEASUREMENTS FOR PAVIAU ENDMEMBERS

Endmembers	# of samples extracted from the scene	Total # of bands	# of bands where $RMSBeta \leq RMSGaussian$	Percentage of bands where $RMSBeta \leq RMSGaussian$ (%)	# of bands where $KLDivBeta \leq KLDivGaussian$	Percentage of bands where $KLDivBeta \leq KLDivGaussian$ (%)
Asphalt	1354	103	102	99.03	102	99.03
Meadows	1044	103	52	50.49	53	51.46
Gravel	1042	103	43	41.75	42	40.78
Trees	962	103	58	56.31	61	59.22
Painted metal sheets	290	103	0	0.00	0	0.00
Bare soil	2223	103	99	96.12	102	99.03
Bitumen	675	103	0	0.00	0	0.00
Self-blocking bricks	490	103	23	22.33	7	6.80
Shadows	183	103	100	97.09	100	97.09

where e_{md} is the reflectance value of the dth band of mth endmember. $B(\cdot)$ is the beta distribution where

$$B(e|\alpha, \beta) = \Gamma(\alpha)\Gamma(\beta)\Gamma(\alpha + \beta)^{-1} e^{\alpha-1} (1-e)^{\beta-1} \quad (3)$$

α_{md} and $\beta_{md} \geq 0$ are the parameters for the beta distribution.

Thus, in the BCM, each pixel is considered a random variable with the distribution of a convex combination of beta-distributed endmembers

$$x_{id} \sim \mathfrak{F}_{\mathfrak{M}}(\cdot \,|\, \mathbf{p}_i, \boldsymbol{\alpha}_d, \boldsymbol{\beta}_d) \quad (4)$$

where

$$\mathfrak{F}_{\mathfrak{M}}(\cdot \,|\, \mathbf{p}_i, \boldsymbol{\alpha}_d, \boldsymbol{\beta}_d) = \sum_{m=1}^{M} p_{im} B(e_{md} \,|\, \alpha_{md}, \beta_{md}) + \epsilon_{id} \quad (5)$$

x_{id} is the spectral value of the dth band of ith data point, M is the number of endmembers, p_{im} is the proportion value of the mth endmember in the ith data point, and ϵ is a noise term. The proportions fulfill nonnegativity and sum-to-one constraints

$$p_{im} \geq 0 \quad (6)$$

$$\sum_{m=1}^{M} p_{im} = 1. \quad (7)$$

However, the resulting distribution of a convex combination of beta distributions is highly complex. Therefore, to reduce the computational complexity, an approximation is used. As seen in [25], one beta distribution, $\mathbf{B}(\cdot|e, f)$, can be used to approximate the convex combination of beta distributions. The parameters e and f of the approximated beta distribution are obtained by equating the mean and variance of the approximated single beta distribution to that of a combination of several beta distributions. Given a set of data $\mathbf{x}_d$ on dth band that is distributed according to the same convex combination of beta distributions (i.e., the same proportion vectors), the parameters f_d and e_d for the approximated beta on band d can be computed using (8) and (9). Note that the approximation is applied on a band-per-band basis

$$f_d = F_d(S_d(1 + F_d)^3)^{-1} - (1 + F_d)^{-1} \quad (8)$$

$$e_d = F_d f_d \quad (9)$$

where

$$F_d = E_d(1 - E_d)^{-1} \quad (10)$$

$E_d = \mathscr{E}(x_{id})$ (the expected value of the data) and $S_d = var(x_{id})$ (the variance of the data).

In order to perform spectral unmixing, given the e_{id} and f_{id} values approximated from the data, and given known beta endmember parameters $\boldsymbol{\alpha}$ and $\boldsymbol{\beta}$ the proportion values can be estimated by determining the proportions that minimize the difference between the two sides of (11) and (12)

$$\frac{e_{id}}{e_{id} + f_{id}} = \sum_{m=1}^{M} p_{im} \frac{\alpha_{md}}{\alpha_{md} + \beta_{md}} \quad (11)$$

$$\frac{e_{id} f_{id}}{(e_{id} + f_{id})^2 (e_{id} + f_{id} + 1)}$$
$$= \sum_{m=1}^{M} p_{im}^2 \frac{\alpha_{md} \beta_{md}}{(\alpha_{md} + \beta_{md})^2 (\alpha_{md} + \beta_{md} + 1)}. \quad (12)$$

The left-hand sides of (11) and (12) are the mean and variance of the beta distributions whose parameters have been estimated from the data. The right-hand sides of (11) and (12) are the mean and variance of the convex combination of M beta distribution with known $\boldsymbol{\alpha}$ and $\boldsymbol{\beta}$ values (obtained from the the known endmember distributions). The task of unmixing then becomes estimating the proportion values, which provide the best fit between the parameters estimated from the data and the convex combination of beta endmember distributions. The proportion values p_{im} can then be determined using either the quadratic programming (QP) approach or the Metropolis–Hastings (MH) sampling method described in Section IV.

IV. BCM-SPECTRAL AND BCM-SPATIAL UNMIXING

Two unmixing approaches are proposed under the BCM framework: BCM-spectral and BCM-spatial approaches. For both methods, in order to unmix a single pixel, additional pixels with identical or similar proportion values need to be identified such that the left-hand side of (11) and (12) can be estimated. The BCM-spectral approach uses only spectral information to identify pixels with similar proportion values. The BCM-spatial approach takes into account both spectral and spatial information. Under each approach, two unmixing algorithms are discussed: 1) a QP approach and 2) an MH sampling approach. Both the QP and MH sampling approaches are methods of moments-type algorithms. For the QP approach, the proportions are estimated by minimizing the difference between the mean estimated from the data and the mean of the convex combination of endmember distributions. For the MH sampling approach, the difference between both the mean and the variance estimated from the data and from the convex combination of endmember distributions is minimized.

A. BCM-Spectral

BCM-spectral approach identifies pixels with similar proportion values to the pixel under test by identifying the K-nearest spectral neighbors. In the current implementation, the K-nearest spectral neighbors are identified using squared Euclidean distance. However, other dissimilarity measures can be used (e.g., spectral angle [26] or spectral information divergence [27]). Using the K-nearest spectral neighbors for each pixel, QP and MH sampling algorithms are developed.

1) QP Method: In the QP approach, the difference between the mean of the K-nearest spectral neighbors for each pixel and the mean from the convex combination of beta endmember distributions is minimized. The objective function can be written as follows:

$$JBCM_{id}^{QP} = \left\| \frac{e_{id}}{e_{id}+f_{id}} - \sum_{m=1}^{M} p_{im} \frac{\alpha_{md}}{\alpha_{md}+\beta_{md}} \right\|_2^2. \quad (13)$$

The K-nearest spectral neighbors for each pixel are regarded as the "source data" and one beta distribution for each dimension with parameters e_{id} and f_{id} from (8) and (9) are estimated using a maximum likelihood approximation of these beta parameters given the source data. Specifically, in the current implementation, MATLAB's *betafit* function is used [19]. The α_{md} and β_{md} are assumed to be known. Then, a QP method was used to minimize (13) and solve for p_{im} given constraints (6) and (7). The pseudo-code for QP unmixing based on the BCM is shown in Algorithm 1.

Algorithm 1: BCM Quadratic Programming Approach

Require: data $\mathbf{x}_i$ for $i = 1, 2, \dots N$, K

1: **for** $i \leftarrow 1$ to N **do**

2:      Identify the K nearest spectral neighbors for pixel $\mathbf{x}_i$, $\mathcal{N}_{\mathbf{x}i}$

3:      Estimate e_{id} and f_{id} using maximum likelihood and $\mathcal{N}_{\mathbf{x}i}$

4:      Return proportion values estimated by minimizing (13) s.t. constraints in (6) & (7) using QP

5: **end for**

---

2) MH Sampling Method: In the MH sampling approach, both the mean and variance of the beta approximation are taken into consideration. The proportion values are estimated by determining the proportions that minimize the difference between the two sides of (11) and (12).

The likelihood function that is maximized can be written as follows:

$$p(E_{id}, S_{id}|\Theta) = \mathcal{N}\left(E_{id} \middle| \sum_{m=1}^{M} p_{im} \frac{\alpha_{md}}{\alpha_{md}+\beta_{md}}, \sigma_{mean} \right)$$
$$\mathcal{N}\left(S_{id} \middle| \sum_{m=1}^{M} p_{im}^2 \frac{\alpha_{md}\beta_{md}}{(\alpha_{md}+\beta_{md})^2(\alpha_{md}+\beta_{md}+1)}, \sigma_{var} \right) \quad (14)$$

where $\Theta = (\boldsymbol{\alpha}, \boldsymbol{\beta}, \sigma_{mean}, \sigma_{var})$, $E_{id} = \mathcal{E}(x_{id})$ is the mean over all K nearest neighbors of pixel i, $S_{id} = var(x_{id})$ is the variance

computed over K nearest neighbors of pixel i, and σ_{mean} and σ_{var} are fixed parameters that are set to weight the relative importance placed on the mean and variance terms in the likelihood.

This likelihood function is maximized by iteratively sampling proportion values. Specifically, proportion values are initialized by drawing samples from a symmetric Dirichlet distribution with α parameters all equal to 1. Then, proposal proportion values for each data are sampled from the symmetric Dirichlet distribution. The proposal proportion values are accepted with some probability given by the acceptance ratio as follows:

$$a_p = min\left\{ \frac{f(\mathbf{E}_i, \mathbf{S}_i|\Theta, \mathbf{p}_i^{new})}{f(\mathbf{E}_i, \mathbf{S}_i|\Theta, \mathbf{p}_i^{old})}, 1 \right\}. \quad (15)$$

The MH sampler estimates the full distribution of possible proportion values for each data point. In (15), $f(\mathbf{E}_i, \mathbf{S}_i|\Theta, \mathbf{p}_i)$ can be interpreted as the likelihood of data point $\mathbf{x}_i$ and its K-nearest neighbors given the known endmember distributions and sampled proportion values

$$f(\mathbf{E}_i, \mathbf{S}_i|\Theta, \mathbf{p}_i) \propto \prod_{d=1}^{D} \mathcal{N}\left(E_{id} \middle| \sum_{m=1}^{M} p_{im} \frac{\alpha_{md}}{\alpha_{md}+\beta_{md}}, \sigma_{mean} \right)$$
$$\mathcal{N}\left(S_{id} \middle| \sum_{m=1}^{M} p_{im}^2 \frac{\alpha_{md}\beta_{md}}{(\alpha_{md}+\beta_{md})^2(\alpha_{md}+\beta_{md}+1)}, \sigma_{var} \right). \quad (16)$$

The pseudo-code for sampling unmixing based on the BCM is summarized in Algorithm 2.

Algorithm 2: BCM Sampling Approach

Require: data $\mathbf{x}_i$ for $i = 1, 2, \dots N$, K

1: **for** $i \leftarrow 1$ to N **do**

2:      Generate an initial proportion sample $\mathbf{p}_i^{old}$ from a uniform Dirichlet distribution

3:      Calculate $Likelihood(0) \leftarrow f(\mathbf{x}_i|\Theta, \mathbf{p}_i^{old})$

4:      Identify the K-nearest neighbors for pixel x_i, $\mathcal{N}_{x_i}$

5:      Estimate e_{id} and f_{id} for each band d using maximum likelihood and $\mathcal{N}_{x_i}$

6:      **for** $t \leftarrow 1$ to maximum number of iterations $tmax$ **do**

7:          Generate a proposal proportion vector, $\mathbf{p}_i^{new}$, from a uniform Dirichlet distribution

8:          Calculate $LikelihoodNew \leftarrow f(\mathbf{x}_i|\Theta, \mathbf{p}_i^{new})$

9:          Calculate the acceptance ratio according to equation (15)

10:         Generate a uniformly-distributed random value, u, on the interval [0, 1]

11:         **if** $u < acceptance\,ratio$ **then**

12:            $Likelihood(t) \leftarrow LikelihoodNew$

13:            $\mathbf{p}_i^{(t)} \leftarrow \mathbf{p}_i^{new}$

14:       **else**

15:             $Likelihood(t) \leftarrow Likelihood(t-1)$

16:             $\mathbf{p}_i^{(t)} \leftarrow \mathbf{p}_i^{old}$

17:       **end if**

18:     **end for**

19: **end for**

B. BCM-Spatial

The BCM-spatial unmixing approach mimics the BCM-spectral approach except for the identification of the K-nearest neighbors. To identify spatial–spectral neighbors, the K-means algorithm is applied to cluster the input image data with location information appended and scaled. The scaling parameter depends on the importance to be placed on the location information versus the spectral values. The image data with scaled location information can be written as

$$\hat{x}_{iL}^T = [\, x_{i1}, x_{i2}, , x_{iD}, s \cdot row_i, s \cdot col_i \,] \qquad (17)$$

where D is the total number of bands and s is the scaling parameter. Here, the traditional K-Means algorithm with the spatial (location) information is called the "spatial K-means approach" for the rest of the paper. After the image data are clustered using the spatial K-means approach, the nearest spectral neighbors that are within each spatial cluster of the data point under consideration are identified. Using these neighbors, the QP and MH sampling algorithms can be completed as described in Sections IV-A1 and IV-A2. Other spatial–spectral clustering algorithms will be considered in future work, including fuzzy local information c-means clustering algorithm (FLICM) [28], modified fuzzy c-means algorithms [29]–[32] and robust fuzzy c-means algorithm with spatial information [33].

C. Computational Complexity

The BCM approaches need computation time to find spectral and spatial neighbors for each pixel. Also, the computation of the data likelihood in the BCM methods requires additional time. To investigate the needed computing time, we ran the BCM-spatial experiments for 10 times and timed each of the main steps. Across the 10 runs, we computed the percentage of time used in each step of the approach. The results are: 1) run K-means—0.43%; 2) find neighbors for each pixel—24.27%; 3) estimate beta parameters for each pixel using MATLAB's *betafit* function—69.04%; and 4) unmixing (obtain proportion values)—6.25%. As can be seen from the above results, the majority of time is taken by identifying the neighbors for each pixel and estimating the beta parameters for each pixel. However, both of these steps can be sped up through the use of parallel computing methods. Namely, both of these steps can be trivially parallelized. Future work will included further exploration on the optimization and improvement of the run speed.

A number of QP approaches with varying levels of computational complexity have been developed in the literature [34]–[36]. In MH sampling approach for unmixing, the most computational consuming step is computing the data log-
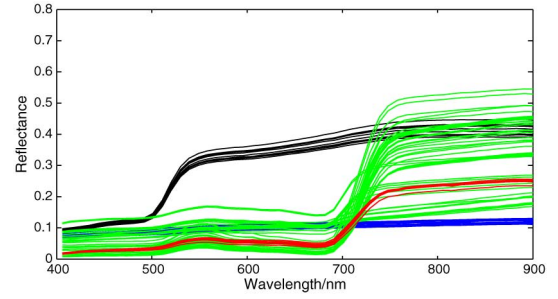

Fig. 4. Four endmember spectra measured using a handheld ASD spectrometer for simulated data. Blue: asphalt; black: yellow curb; red: grass; green: oak leaves.

likelihood based on the data-likelihood shown in (16). Taking the log, the log-likelihood term is shown as follows:

$$loglikelihood_{id} = -\frac{\left(E_{id} - \sum_{j=1}^{M} p_{ij} \frac{\alpha_{jd}}{\alpha_{jd}+\beta_{jd}} \right)^2}{2\sigma_{mean}^2}$$
$$-\frac{\left(S_{id} - \sum_{j=1}^{M} p_{ij}^2 \frac{\alpha_{jd}\beta_{jd}}{\left(\alpha_{jd}+\beta_{jd}\right)^2 \left(\alpha_{jd}+\beta_{jd}+1\right)} \right)^2}{2\sigma_{var}^2}.$$
$$(18)$$

The computational complexity for computing the log-likelihood in a single iteration for each pixel is $O(DM)$, M is the number of endmembers, and D is the number of bands. The computational complexity of I iterations across N data points is $O(INDM)$, where N is the number of pixels and I is the number of iterations.

Running times for simulated data experiments are also included in Section V.

V. EXPERIMENTS AND RESULTS

A. Data Sets

The proposed unmixing algorithms were tested on both simulated data and real hyperspectral imagery. Two sets of simulated data were constructed to be able to quantitatively evaluate the methods since the true proportion values would be known. Real images are tested to prove the effectiveness of the proposed unmixing algorithms on measured HSI imagery.

The first set of simulated data were constructed from four endmembers: 1) asphalt (with 10 samples), 2) yellow curb (10 samples), 3) grass (10 samples), and 4) oak leaves (50 samples) whose samples were measured using a handheld ASD spectrometer at the campus of the University of South Mississippi-Gulfpark [18]. The wavelengths range from 400 to 900 nm. The endmember signatures are shown in Fig. 4. Note that for Grass and oak leaves, the basic spectral shapes of the endmember spectral signature are similar but with significantly different variance.

The first simulated data were arranged in 100×100 images that were composed of 47×47 pixel squares on each of the four corners, consisting of samples from only one of the four endmembers distributions. The center of 6×6 regions consists of mixtures of samples from all four endmember distributions with randomly generated proportions (sampled from a uniform
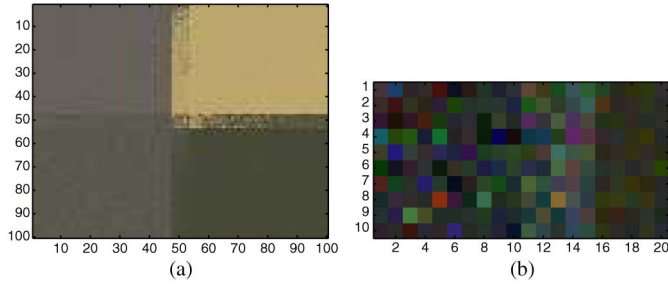
Fig. 5. RGB image of simulated data sets. (a) Simulated data set 1 and (b) simulated data set 2.
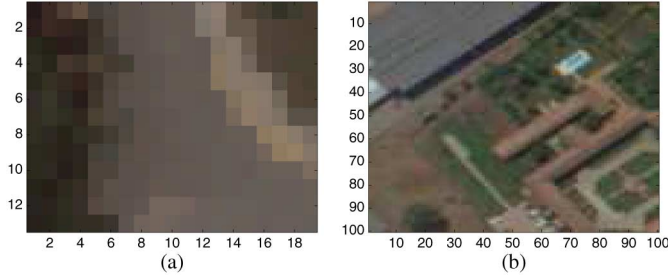

Fig. 6. RGB image of real data sets. (a) 13×19 subset of the Gulfport data and (b) 100×100 subset of the Pavia University data.

Dirichlet distribution). Also, four 47×3 mixed pixel regions were constructed that consist of mixtures of samples from only the two nearby endmember distributions. Gaussian noise with a variance 0.001 ($SNR_{db} = 19.89$ db) were constructed. RGB images of simulated data with noise are shown in Fig. 5(a).

The second set of simulated data are constructed using eight endmembers pulled from the Pavia University imagery [20]: asphalt, meadows, gravel, trees, painted metal sheets, bare soil, bitumen, and self-blocking bricks. A description of the Pavia University data set can be seen in Section II. The simulated images were 10×20 in size, which consists of four "sections" with the size of 10×5 lined up horizontally. Within each section, two of the endmembers are chosen and mixed with proportions drawn from a uniform Dirichlet distribution. An RGB image of the simulated data can be seen in Fig. 5(b).

The unmixing experiments were also applied to two real hyperspectral data sets. The first image was collected in Longbeach, MS. An RGB image of the hyperspectral image clip (13×19) used is shown in Fig. 6(a). This particular image clip was chosen as several true endmember samples for all of the materials in this scene were collected with a hand-held ASD spectrometer. Thus, for this image, the endmember distributions are known and spectral unmixing (given the known endmember distributions) can be performed.

The second real data set comes from the Pavia University scene [20] of size 100×100. Four endmembers are obtained by extracting samples from the data: water, buildings and dirt, vegetation, and shadow [2]. Fig. 6(b) shows the RGB image of the data set. This image was chosen for comparison with the results in [2].

B. Review: NCM

The NCM [12], [13] is the most commonly discussed *endmember as distributions* spectral variability approach in the
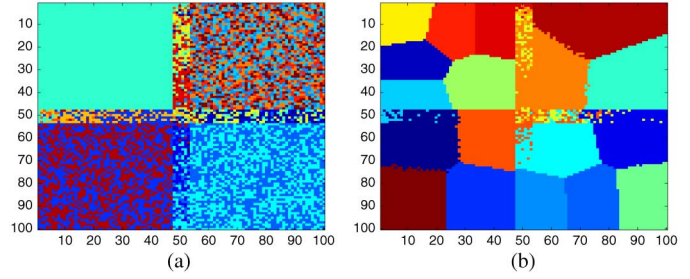

Fig. 7. Cluster results of simulated data by (a) K-means and (b) spatial K-means.

literature. In the NCM, endmembers are represented using multivariate Gaussian distributions. In this paper, NCM methods are used as a comparison to the BCMs in these experimental results. As such, a review of the NCM unmixing algorithms used for comparison is included here.

Two approaches of NCM unmixing, a QP approach and an MH sampling approach, are implemented. In the NCM-QP approach, the objective function can be written as

$$ JNCM_{id}^{QP} = \|\mathbf{X} - \mathbf{PE}\|^2 = \mathbf{X}^T\mathbf{X} - 2\mathbf{X}^T\mathbf{PE} + \mathbf{P}^T\mathbf{E}^T\mathbf{EP} \tag{19} $$

where $\mathbf{X}$ is the data and $\mathbf{E}$ is the mean value of the endmembers. Proportions $\mathbf{P}$ are estimated by minimizing $JNCM_{id}^{QP}$ with nonnegativity and sum-to-one constraints. In the NCM-MH approach, proportion values are sampled from a Dirichlet distribution, and then updated according to the acceptance rate $a_p = min\left\{\frac{f(\mathbf{x}_i|\mathbf{E},\mathbf{p}_i^{new})}{f(\mathbf{x}_i|\mathbf{E},\mathbf{p}_i^{old})}, 1\right\}$ where $f(\mathbf{x}_i|\mathbf{E}, \mathbf{p}_i) = \mathcal{N}(\mathbf{p}_i\mathbf{E}, \sum_{m=1}^{M} p_{im}^2 \mathbf{S}_m)$ is the likelihood of the data point given the known endmember and sampled proportion values, $\mathbf{x}_i$ is the ith data point, and $\mathbf{S}_m$ is the variance of the mth endmember. This is a simplification of the approach presented in [15] in which only one set of endmembers is used and only the proportions are updated.

C. Simulated Data Results

The first step in all four algorithms is to identify the K-nearest neighbors for each pixel. In the BCM-spatial approaches, this is done using the spatial K-means approach described. A comparison of a K-means clustering results and a spatial K-means clustering result of the simulated data is shown in Fig. 7. As can be observed, the spatial K-means approach is able to group neighboring pixels while distinguishing between the four major endmember regions in the simulated imagery.

The BCM-spatial QP and MH sampling approaches were applied to the simulated imagery. For comparison, the fully constrained least squares (FCLS) linear spectral mixture analysis method [37], [38] (which does not incorporate endmember variability) is used to unmix the imagery. The endmembers used in FCLS are the mean values from the endmember spectra. Also, an NCM-based approach is compared to the BCM results [15]. Specifically, only the proportion update step in [15] is applied for a single set of endmember distributions. In all experiments below, $\sigma_{mean} = 0.001$, $\sigma_{var} = 100$, and $s = 100$.

Unmixing results are presented by proportion maps plotted based on proportion values estimated from the unmixing algorithms, and by comparison of proportion error values, $PError$,

TABLE II
MEAN OVER 10 RUNS OF THE AVERAGE PER-PIXEL PER-ENDMEMBER PROPORTION
ERROR FOR SIMULATED DATA

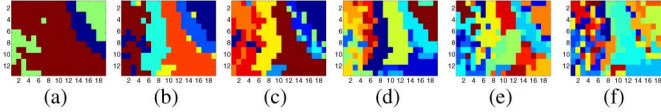| Method	PError	
	Simulated dataset 1	Simulated dataset 2
FCLS	8.685E-3	0.1186
NCM quadprog	8.699E-3	0.1112
NCM sampling	8.834E-3	0.1167
BCM-spectral quadprog	**8.259E-3**	**0.0328**
BCM-spectral sampling	**8.468E-3**	**0.0425**
BCM-spatial quadprog	**8.177E-3**	**0.0316**
BCM-spatial sampling	**8.452E-3**	**0.0337**

Fig. 8. Gulfport hyperspectral image data cluster result of spatial K-means when cluster number equals (a) 3; (b) 6; (c) 9; (d) 15; (e) 20; and (f) 30.
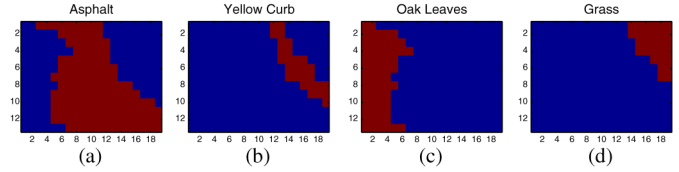

Fig. 9. Manual ground truth of gulfport data set: (a) asphalt; (b) yellow curb; (c) oak leaves; and (d) grass.
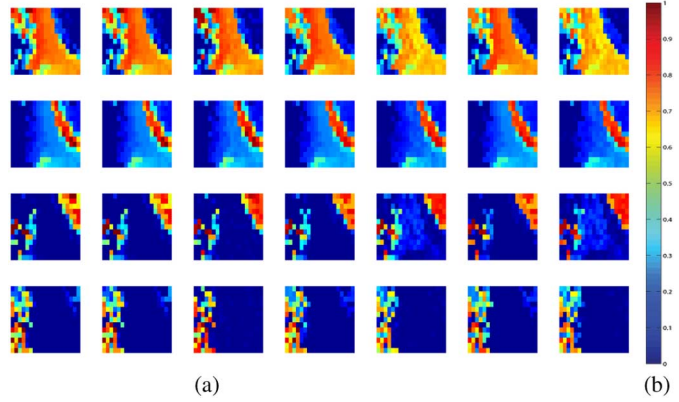

Fig. 10. (a) Unmixing results of asphalt, yellow curb, grass, and oak leaves in gulfport scene by (from left to right by column) FCLS, Gaussian QP, Gaussian sampling, BCM-spectral QP, BCM-spectral sampling, BCM-spatial QP, and BCM-spatial sampling and (b) colorbar.

across different unmixing methods if true proportion values are known. Pixel-wise proportion error values are computed according to $PError_{pixel_i} = \|Ptrue_i - Pestimate_i\|_2$, where $i = 1, \ldots, N$, N is the total number of pixels, $Ptrue$ is the true proportion values, $Pestimate$ is the estimated proportion values, and the $\|\cdot\|_2$ denotes l_2 norm between the two. The proportion error mean values are then calculated using $PError_{pixel_i}$ values divided by the number of endmembers M, representing the proportion error across each pixel for each endmember. The average error over 10 runs is shown in the following proportion error table (Table II).

It can be observed from the table that the traditional FCLS method, which does not account for endmember variability, yields a relative high error in estimated proportion when compared with true proportions values. BCM QP and sampling methods, on the other hand, yield low error values on both simulated data, where simulated data 1 consists of pure pixels and simulated data 2 consists of mixed pixels with proportions chosen from a Dirichlet distribution. Also, since simulated data set 2 consists of endmembers that are better fit to a beta distribution (see Table I), BCM approaches performs significantly better than FCLS and NCM approaches.

The running times for these methods were measured and the average among 10 runs on the 100×100 simulated image were recorded. FCLS took 5 s, NCM-quadprog took 20 s, NCM-sampling took 260 s, BCM-spectral method took 2500 s, and BCM-spatial method took 3000 s. Note that these running times were measured on a desktop PC with Intel i7 3.20 GHz processor and 12 GB RAM. Code was not optimized for running time and the running times are provided for relative comparisons only.

D. Real Hyperspectral Imagery Results

The proposed BCM algorithms were also tested on measured HSI data and compared to an NCM QP approach, NCM sampling approach, BCM QP approach, and BCM sampling approach with spectral neighbors [15], [24]. The ideal spatial cluster should cluster the image into small circle-shape clusters so that they incorporate spatial information, yet consist of enough neighbors

within each cluster for neighbor identification. For the spatial quadratic approaches, 20 spatial clusters were identified and 6 neighbors are identified. Twenty clusters were chosen manually by comparing several results across different numbers of clusters, as shown in Fig. 8.

For the BCM-spatial sampling approaches, six spatial clusters were identified and six neighbors are identified within each cluster.

Ground truth of the Gulfport image data set is drawn manually for asphalt, yellow curb, oak leaves, and grass, as shown in Fig. 9.

As shown in Fig. 10(d)–(g), the pixels corresponding to asphalt present stronger values in the proportion maps when compared with the FCLS and NCM methods. All methods are able to separate the yellow curb endmember from other endmembers as seen in Fig. 10, but proportion maps from BCM-spatial methods in (f) and (g) show larger proportion values over the yellow curb area smaller values over other pixels.

Table III presents quantitative measurements of the proportion error values of unmixing results against the manual ground truth as shown in Fig. 9. The pixel-wise proportion error values are computed similar to Table II. It can be observed that as compared with FCLS and NCM methods, the proposed BCM methods produce smaller proportion errors.

The unmixing results of the grass endmember from the FCLS and NCM methods as the proportion maps show large proportion values over both the grass region and the oak leaves region. As mentioned before, the grass and oak leaves endmembers have similar spectral shapes but a different variance. BCM methods appropriately separated the grass and oak leaves regions.

It can also be observed that, when comparing the BCM-spatial QP and BCM-spatial sampling methods to their corresponding

TABLE III
MEAN OVER 10 RUNS OF THE AVERAGE PER-PIXEL PER-ENDMEMBER PROPORTION
ERROR FOR REAL GULFPORT DATA WITH MANUAL GROUND TRUTH

Method	PError
FCLS	0.1527
NCM quadprog	0.1517
NCM sampling	0.1619
BCM-spectral quadprog	**0.1497**
BCM-spectral sampling	**0.1498**
BCM-spatial quadprog	**0.1507**
BCM-spatial sampling	**0.1433**

TABLE IV
ERROR MEAN VALUES AGAINST MEDIAN OF THE PROPORTION MAPS FOR
PAVIAU DATA SET

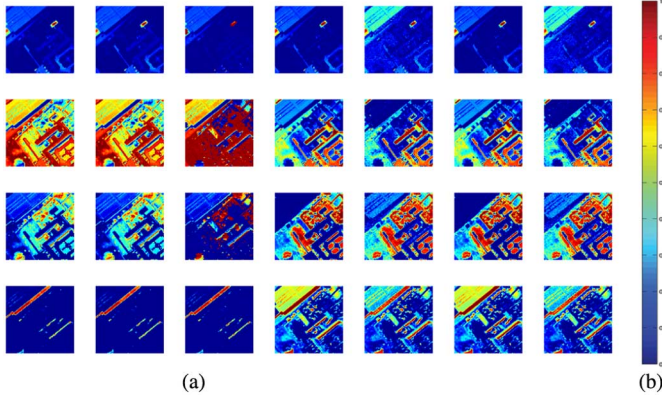| Method	PError
FCLS	0.1534
NCM quadprog	0.1533
NCM sampling	0.1794
BCM-spectral quadprog	**0.0095**
BCM-spectral sampling	**0.0022**
BCM-spatial quadprog	**0.0096**
BCM-spatial sampling	**0.0023**

Fig. 11. (a) Unmixing results of water, buildings and dirt, vegetation and shadow in the PaviaU scene by (from left to right by column) FCLS, Gaussian QP, Gaussian sampling, BCM-spectral QP, BCM-spectral sampling, BCM-spatial QP, and BCM-spatial sampling and (b) colorbar.

values are then calculated using $PError_{pixel_i}$ values divided by the number of endmembers M, representing the proportion error across each pixel for each endmember. The error mean values for FCLS, Gaussian QP, Gaussian MH Sampling, BCM-spectral QP, BCM-spectral sampling, BCM-spatial QP, and BCM-spatial sampling are listed in Table IV.

VI. CONCLUSION AND FUTURE WORK

The BCM-spatial and BCM-spectral unmixing algorithms presented here assume beta-distributed endmembers given the LMM. The BCM approaches are shown to be able to successfully perform unmixing on both simulated data and real hyperspectral imagery.

Current ongoing work includes a different approach for the BCM that does not require the estimation of spectral neighbors. This approach uses an MH sampler applied directly to the full likelihood of the data given the model with corresponding priors, closely mirroring the approach in [14] for the NCM.

Current K nearest neighbor approach may hurt anomalous pixels, and while the current algorithms are well-suited for unmixing large background materials, future work may include an anomaly detection step prior to unmixing such that these pixels can be addressed appropriately without the use of K-NN approach.

Other spatial–spectral clustering and superpixel approaches will also be considered in future work, such as FLICM [28], modified fuzzy c-means algorithms [29]–[32] and robust fuzzy c-means algorithm with spatial information [33]. In order to incorporate spatial information, superpixel and clustering algorithms are effective in obtaining data clusters, yet if all neighbors in the clusters are used for unmixing, the resulting proportion maps may conform to the shapes of the cluster labels. Thus, future work will include the development of superpixel-based spatial–spectral nearest neighbor approaches.

Besides, hyperspectral data are very correlated across the spectral domain, and future work in NCM and beta unmixing approaches need to address endmember covariance.

Another future work item could be the repeated application of randomly initialized endmember extraction algorithms to generate endmember sets and distributions. Related work can be seen in [39] and [40].

In order to address computation time, future work in implementing the proposed BCM approaches using parallel computing methods will be investigated. In particular, the current implementation estimates beta parameters for each pixel using a loop and, however, as each data point is independent in this computation, this step can be trivially parallelized.

spectral approaches, very little speckle in the proportion values of oak leaves region can be observed. This is due to the fact that BCM-spatial algorithms take into account local spatial information of the image.

Another real data set of size 100×100 from Pavia University scene is tested for the unmixing approaches. Four endmembers are obtained by extracting samples from the data: water, buildings and dirt, vegetation, and shadow [2]. Fig. 6(b) shows the RGB image of the data set. Fig. 11 presents the proportion maps for FCLS, NCM, and BCM methods. The proportion maps are scaled to [0, 1] using the same colorbar as above, as shown in Fig. 11.

All unmixing approaches for the PaviaU data set are able to accurately identify the water and shadow as illustrated by the proportion maps. For both vegetation endmember and the buildings/dirt endmember, the proportion maps estimated by the BCM approaches estimate large proportion values and clear boundaries over the buildings and vegetation area as compared to FCLS and NCM approaches.

Also, following the approach in [2], we have computed the error between the estimated proportion maps and the median of the proportion maps over all methods (with the median being regarded as the desired output). The total error mean values are computed according to $PError_{pixel_i} = \|Pmedian_i - Pestimate_i\|_2$, where $i = 1, \ldots, N$, N is the total number of pixels, $Pmedian$ is the median proportion values across all methods, $Pestimate$ is the estimated proportion values, and the $\|\cdot\|_2$ denotes l_2 norm between the two. The proportion error mean

Furthermore, scattering between endmembers and intimate mixtures in the scene can lead to nonlinear mixing. Thus, development of nonlinear BCM approaches can be further future work as well.

REFERENCES

[1] C. Song, "Spectral mixture analysis for subpixel vegetation fractions in the urban environment: How to incorporate endmember variability?" *Remote Sens. Environ.*, vol. 95, no. 2, pp. 248–263, Mar. 2005.

[2] A. Zare and K. Ho, "Endmember variability in hyperspectral analysis: Addressing spectral variability during spectral unmixing," *IEEE Signal Process. Mag.*, vol. 31, no. 1, pp. 95–104, Jan. 2014.

[3] X. Jia, C. Dey, D. Fraser, L. Lymburner, and A. Lewis, "Controlled spectral unmixing using extended support vector machines," in *Proc. 2nd Workshop Hyperspectral Image Signal Process.: Evol. Remote Sens. (WHISPERS)*, 2010, pp. 1–4.

[4] X. Li, L. Wang, and X. Jia, "Spectral unmixing based on improved extended support vector machines," in *Proc. Int. Geosci. Remote Sens. Symp. (IGARSS)*, 2012, pp. 4118–4121.

[5] D. Roberts *et al.*, "Mapping chaparral in the Santa Monica mountains using multiple endmember spectral mixture models," *Remote Sens. Environ.*, vol. 65, no. 3, pp. 267–279, Sep. 1998.

[6] J.-P. Combe *et al.*, "Analysis of omega/mars express data hyperspectral data using a multiple-endmember linear spectral unmixing model (MELSUM): Methodology and first results," *Planet. Space Sci.*, vol. 56, pp. 951–975, 2008.

[7] G. Asner, M. Bustamante, and A. Townsend, "Scale dependence of biophysical structure in deforested areas bordering the Tapajos National Forest, Central Amazon," *Remote Sens. Environ.*, vol. 87, no. 4, pp. 507–520, 2003.

[8] C. Bateson, G. Asner, and C. Wessman, "Endmember bundles: A new approach to incorporating endmember variability into spectral mixture analysis," *IEEE Trans. Geosci. Remote Sens.*, vol. 38, no. 2, pp. 1083–1094, Mar. 2000.

[9] B. Somers, G. P. Asner, L. Tits, and P. Coppin, "Endmember variability in spectral mixture analysis: A review," *Remote Sens. Environ.*, vol. 115, no. 7, pp. 1603–1616, Jul. 2011.

[10] J. Jin, B. Wang, and L. Zhang, "A novel approach based on fisher discriminant null space for decomposition of mixed pixels in hyperspectral imagery," *IEEE Geosci. Remote Sens. Lett.*, vol. 7, no. 4, pp. 699–703, Oct. 2010.

[11] P. Dennison and D. Roberts, "Multiple endmember spectral mixture analysis using endmember average RSME," *Remote Sens. Environ.*, vol. 87, no. 2–3, pp. 123–135, Oct. 2003.

[12] D. Stein, "Application of the normal compositional model to the analysis of hyperspectral imagery," in *Proc. Workshop Adv. Tech. Anal. Remotely Sens. Data*, 2003, pp. 44–51.

[13] M. T. Eismann and D. W. J. Stein, *Stochastic Mixture Modeling*. Hoboken, NJ, USA: Wiley, 2006, pp. 107–148.

[14] O. Eches, N. Dobigeon, C. Mailhes, and J.-Y. Tourneret, "Bayesian estimation of linear mixtures using the normal compositional model: Application to hyperspectral imagery," *IEEE Trans. Image Process.*, vol. 19, no. 6, pp. 1403–1413, Jun. 2010.

[15] A. Zare, P. Gader, and G. Casella, "Sampling piecewise convex unmixing and endmember extraction," *IEEE Trans. Geosci. Remote Sens.*, vol. 51, no. 3, pp. 1655–1665, Mar. 2013.

[16] P. Bosdogianni, M. Petrou, and J. Kittler, "Mixture models with higher order moments," *IEEE Trans. Geosci. Remote Sens.*, vol. 35, no. 2, pp. 341–353, Mar. 1997.

[17] M. B. Wilk and R. Gnanadesikan, "Probability plotting methods for the analysis of data," *Biometrika*, vol. 55, no. 1, pp. 1–17, 1968.

[18] P. Gader, A. Zare, R. Close, G. Tuell, and J. Aitken, "Hyperspectral and lidar airborne data set," Univ. Florida, Gainesville, FL, USA, Tech. Rep. REP-2013-570, 2013.

[19] *Matlab Statistics Toolbox 2013a*. Natick, MA, USA: The Mathworks Inc.

[20] S. Holzwarth *et al.*, "Hysens-DAIS 7915/ROSIS imaging spectrometers at DLR," in *Proc. 3rd EARSel. Workshop Imag. Spectrosc.*, May 2003, pp. 3–14.

[21] S. Kullback and R. A. Leibler, "On Information and sufficiency," *Ann. Math. Stat.*, vol. 22, no. 1, pp. 79–86, 1951.

[22] N. Keshava and J. Mustard, "Spectral unmixing," *IEEE Signal Process. Mag.*, vol. 19, no. 1, pp. 44–57, Jan. 2002.

[23] J. Bioucas-Dias *et al.*, "Hyperspectral unmixing overview: Geometrical, statistical, and sparse regression-based approaches," *IEEE J. Sel. Topics Appl. Earth Observ.*, vol. 5, no. 2, pp. 354–379, Apr. 2012.

[24] A. Zare, P. Gader, D. Drashnikov, and T. Glenn, "Beta compositional model for hyperspectral unmixing," in *Proc. 5th Workshop Hyperspectral Image Signal Process.: Evol. Remote Sens. (WHISPERS)*, 2013.

[25] B. Jhannessona and N. Giria, "On approximations involving the beta distribution," *Commun. Stat. Simul. Comput.*, vol. 24, pp. 489–503, 1995.

[26] N. Keshava, "Distance metrics and band selection in hyperspectral processing with applications to material identification and spectral libraries," *IEEE Trans. Geosci. Remote Sens.*, vol. 42, no. 7, pp. 1552–1565, Jul. 2004.

[27] C.-I. Chang, "Spectral information divergence for hyperspectral image analysis," in *Proc. IEEE Geosci. Remote Sens. Symp. (IGARSS)*, 1999, vol. 1, pp. 509–511.

[28] S. Krinidis and V. Chatzis, "A robust fuzzy local information c-means clustering algorithm," *IEEE Trans. Image Process.*, vol. 19, no. 5, pp. 1328–1337, May 2010.

[29] N. Mohamed, M. Ahmed, and A. Farag, "Modified fuzzy c-mean in medical image segmentation," in *Proc. IEEE Int. Conf. Acoust. Speech, Signal Process.*, 1999, vol. 6, pp. 3429–3432.

[30] M. Ahmed, S. Yamany, N. Mohamed, A. Farag, and T. Moriarty, "A modified fuzzy c-means algorithm for bias field estimation and segmentation of MRI data," *IEEE Trans. Med. Imag.*, vol. 21, no. 3, pp. 193–199, Mar. 2002.

[31] L. Szilagyi, Z. Benyo, S. Szilagyi, and H. S. Adam, "MR brain image segmentation using an enhanced fuzzy c-means algorithm," in *Proc. 25th Annu. Int. Conf. Eng. Med. Biol. Soc.*, 2003, vol. 1, pp. 724–726.

[32] B. Yan, M. Xie, J.-J. Gao, and W. Zhao, "A fuzzy c-means based algorithm for bias field estimation and segmentation of MR images," in *Proc. Int. Conf. Apperceiving Comput. Intell. Anal. (ICACIA)*, 2010, pp. 307–310.

[33] S. F. G. Saeed Fazli, "Robust fuzzy c-means with spatial information for segmentation of brain magnetic resonance images," *Int. J. Sci. Eng. Invest.*, vol. 2, no. 12, pp. 100–105, Jan. 2013.

[34] F. Delbos and J. C. Gilbert, "Global linear convergence of an augmented Lagrangian algorithm to solve convex quadratic optimization problems," *J. Convex Anal.*, vol. 12, no. 1, pp. 45–69, 2005.

[35] K. G. Murty and F.-T. Yu, *Linear Complementarity, Linear and Nonlinear Programming*. Berlin: Heldermann Verlag, 1988.

[36] G. B. Dantzig and M. N. Thapa, *Linear Programming 2: Theory and Extensions*. New York, NY, USA: Springer, 2003.

[37] D. Heinz and C.-I. Chang, "Fully constrained least squares linear spectral mixture analysis method for material quantification in hyperspectral imagery," *IEEE Trans. Geosci. Remote Sens.*, vol. 39, no. 3, pp. 529–545, Mar. 2001.

[38] I. Gerg. (2012). *Matlab Hyperspectral Toolbox* [Online]. Available: http://sourceforge.net/projects/matlabhyperspec/

[39] A. Zare, P. Gader, T. Allgire, D. Drashnikov, and R. Close, "Bootstrapping for piece-wise convex endmember distribution detection," in *Proc. 4th Workshop Hyperspectral Image Signal Process.: Evol. Remote Sens. (WHISPERS)*, Jun. 2012.

[40] B. Somers, M. Zortea, A. Plaza, and G. Asner, "Automated extraction of image-based endmember bundles for improved spectral unmixing," *IEEE J. Sel. Topics Appl. Earth Observ.*, vol. 5, no. 2, pp. 396–408, Apr. 2012.

Xiaoxiao Du (S'12) received the B.Eng. (Hons.) degree in electrical engineering from Zhejiang University, Hangzhou, China with Chu Kochen Honors Certificate, in 2011, and the M.S. degree in electrical engineering from the University of Missouri, Columbia, MO, USA, in 2013. She is currently pursuing the Ph.D. degree in electrical and computer engineering at the same university.

She is a Graduate Research Assistant with the Department of Electrical and Computer Engineering, University of Missouri. Her research interest include machine learning, hyperspectral image analysis, remote sensing, pattern recognition, and signal and image processing.

Alina Zare (S'07–M'08–SM'14) received the Ph.D. degree in computer and information science and engineering from the University of Florida, Gainesville, FL, USA, in 2008.

She is currently an Assistant Professor with the Department of Electrical and Computer Engineering, University of Missouri, Columbia, MO, USA. Her research interests include machine learning, Bayesian methods, sparsity promotion, image analysis, pattern recognition, hyperspectral image analysis, and human geography.

Paul Gader (M'86–SM'99–F'11) received the Ph.D. degree in mathematics for image-processing-related research from the University of Florida, Gainesville, FL, USA, in 1986.

He was a Senior Research Scientist with Honeywell, Morristown, NJ, USA, a Research Engineer and Manager with the Environmental Research Institute of Michigan, Ann Arbor, MI, USA, and a Faculty Member with the University of Wisconsin Oshkosh, Oshkosh, WI, USA, the University of Missouri, Columbia, MO, USA, and the University of Florida, where he is currently a Professor and the Interim Chair with the Department of Computer and Information Science and Engineering. He has published hundreds of refereed journal and conference papers. His research interests include a wide variety of theoretical and applied research problems including fast computing with linear algebra, mathematical morphology, fuzzy sets, Bayesian methods, handwriting recognition, automatic target recognition, biomedical image analysis, landmine detection, human geography, and hyperspectral and light detection and ranging image analysis projects.

Dr. Gader's work in landmine detection has led to his latest membership in IEEE.

Dmitri Dranishnikov received the B.S. degree in mathematics from the University of Florida, Gainesville, FL, USA, in 2008, and the Ph.D. degree in computer engineering from the same university, in 2014.

He is a Research Assistant with the Department of Computer and Information Science and Engineering, University of Florida. His research interests include machine learning, hyperspectral image analysis, and probability theory.